Global structure of magnetotail reconnection revealed by mining space magnetometer data

G. K. Stephens[1], M. I. Sitnov[1], R. S. Weigel[2], D. L. Turner[1], N. A. Tsyganenko[3], A. J. Rogers[4], K. Genestreti[5], and J. A. Slavin[6]

[1]The Johns Hopkins University Applied Physics Laboratory, Laurel, MD 20723, USA
[2]George Mason University, Fairfax, VA 22030, USA
[3]Saint-Petersburg State University, Saint-Petersburg, Russia
[4]University of New Hampshire, Durham, NH, USA
[5]Space Science and Engineering, Southwest Research Institute, Durham, NH, USA
[6]Department of Climate and Space Sciences and Engineering, University of Michigan, Ann Arbor, MI, USA

Key Points:

- Global structure of magnetotail reconnection inferred from data mining matches its locations revealed by in-situ observations
- Reconstructed magnetotail reconnection structures include X- and O-lines, as well as magnetic nulls
- Reconstructed multiscale current sheet structure supports its formation mechanism by quasi-adiabatic ion motions

Corresponding author: Grant K. Stephens, `Grant.Stephens@jhuapl.edu`

Abstract

Reconnection in the magnetotail occurs along so-called X-lines, where magnetic field lines tear and detach from plasma on microscopic spatial scales (comparable to particle gyroradii). In 2017–2020 the Magnetospheric MultiScale (MMS) mission detected X-lines in the magnetotail enabling their investigation on local scales. However, the global structure and evolution of these X-lines, critical for understanding their formation and total energy conversion mechanisms, remained virtually unknown because of the intrinsically local nature of observations and the extreme sparsity of concurrent data. Here we show that mining a multi-mission archive of space magnetometer data collected over the last 25+ years and then fitting a magnetic field representation modeled using flexible basis-functions, faithfully reconstructs the global pattern of X-lines; 24 of the 26 modeled X-lines match ($B_z = 0$ isocontours are within ~ 2 Earth radii or R_E) or nearly match ($B_z = 2$ nT isocontours are within $\sim 2R_E$) the locations of the MMS encountered reconnection sites.

Plain Language Summary

Magnetic reconnection is a fundamental process in plasmas which couples microscopic scales ($\sim$electron to proton gyroradii) to explosive macroscopic phenomena many orders of magnitude larger, such as solar flares and geomagnetic storms/substorms. Reconnection forms along "X-lines", rifts where oppositely directed magnetic field lines are forced together. In the Earth's magnetosphere, reconnection has been observed by satellites at isolated locations; however, the large-scale structure of X-lines and their time evolution remains unknown because of the rarity and local nature of observations. Here, ground based measurements of geomagnetic activity and solar wind measurements are used to data-mine 25+ years of magnetometer data from 22 Earth-orbiting satellites, which are then utilized to reconstruct the global magnetic field associated with X-lines in Earth's magnetosphere. We show that these reconstructions pinpoint the reconnection locations by verifying their consistency with direct spacecraft observations.

1 Introduction

X-lines are one of the most fundamental structures in magnetized plasmas, particularly in space, where they link global or even astronomical scale processes to those on the single particle orbit scale, thereby allowing those microscale processes to shape the universe (Ji et al., 2022). Dungey (1961) suggested that the interaction between Earth's magnetic dipole and the solar wind causes reconnection of magnetic field lines on both the day and nightsides of Earth's magnetosphere. The shape of these reconnecting field lines resembles the letter "X" and extends tens of Earth radii ($R_E = 6,371.2$ kilometers) in the dawn-dusk direction thus forming X-lines (Figure 1). An X-line divides space into four sectors. In one pair of opposing sectors, the magnetic field and plasma converge towards the center of the X while in the other pair they are rapidly ejected from it. This reconnection process transforms energy stored in the magnetic field into particle kinetic and thermal energy, making it an efficient energy converter and particle accelerator (Ji et al., 2022). X-lines couple kinetic processes on proton and even electron gyroradius scales ($\lesssim 0.01R_E$) (Torbert et al., 2018) to space weather phenomena on global scales: such as solar flares, coronal mass ejections, and magnetospheric storms and substorms ($\sim 10R_E$) (Camporeale, 2019). This range of scales is so immense that its modeling has become one of the major challenges for nascent exascale computing (Ji et al., 2022).

While the microscale physics of reconnection in the magnetosphere has been studied in detail using recent multi-probe satellite missions (Angelopoulos et al., 2008; Burch et al., 2016; Burch et al., 2016; Torbert et al., 2018), its global structure is difficult to infer from data due to their paucity (rarity and locality): at any moment the huge volume of the magnetosphere ($\gtrsim 10^5 {R_E}^3$) is probed by less than a dozen spacecraft (Sitnov et al., 2019). Understanding the global structure of reconnection is fundamental for determining substorm triggering mechanisms (Sitnov et al., 2019) and the total energy conversion during storms and substorms (Angelopoulos et al., 2013; Angelopoulos et al., 2020). Further, if X-line maps can be constructed from data, these maps could guide

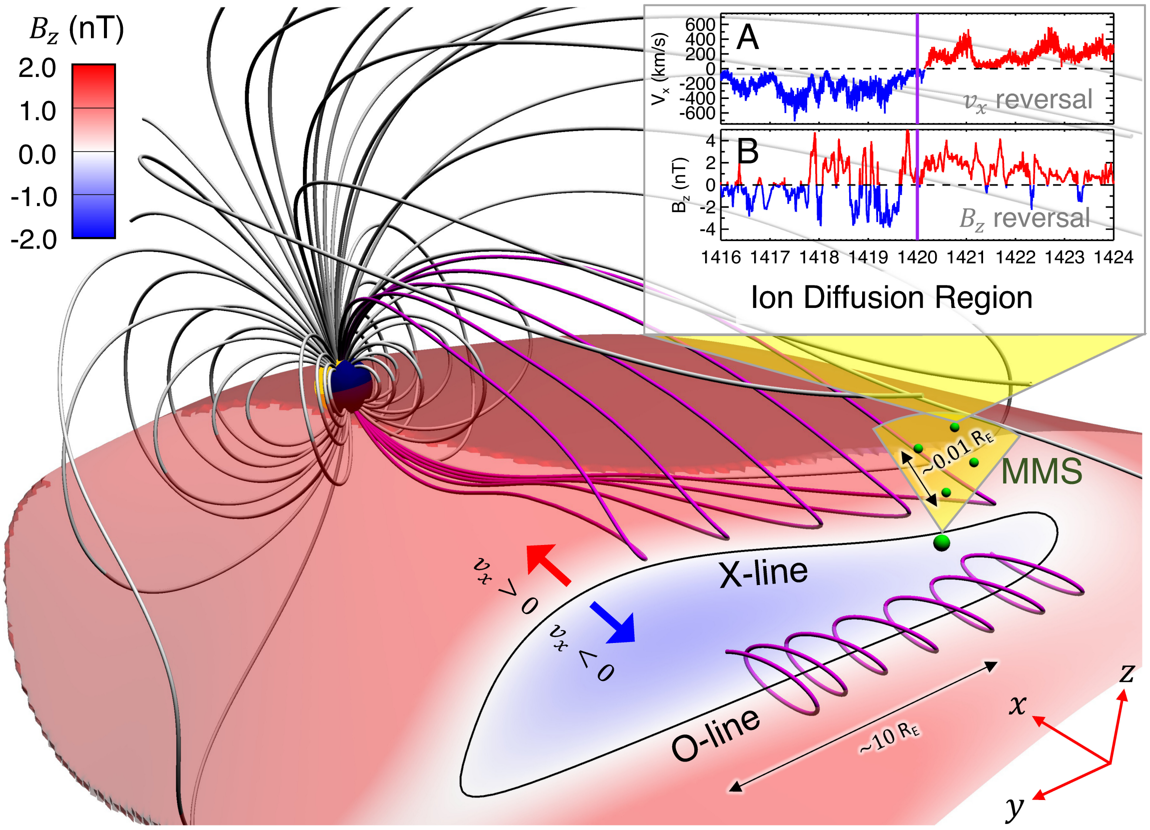

Figure 1. 3D global picture of the magnetosphere and local MMS observations for 5 August 2020 (event Y in Table S2) in GSM coordinates. It shows that the data mining reconstructed X-line hits one of 26 ion diffusion region (IDR) encounters observed by the MMS mission during 2017–2020. It includes selected field lines and the color coded magnetic field distribution, B_z, sampled at the center of the tail current sheet taking into account deformation effects caused by the tilt angle of the Earth's dipole axis as is detailed in the Supporting Information (SI). The $B_z = 0$ isocontour is shown by the black line (the color table is saturated at $|B_z| = 2$ nT to better reveal the isocontour). The inset shows key IDR parameters: (A) the proton bulk flow velocity component v_x and (B) the magnetic field B_z, from the MMS4 probe (the small green spheres show the MMS tetrahedral configuration) whose location is marked by the larger green sphere near the equatorial plane. The purple vertical line marks the reconstruction moment, 5 August 2020, 14:20 UT. The 3D visualizations are constructed using the VisIt visualization tool (Childs et al., 2012).

large-scale magnetohydrodynamic simulations of the magnetosphere by introducing a non-zero resistivity at their locations (Birn et al., 1996).

On the dayside, the X-line location can be readily estimated from the global geometry of the solar wind and Earth's magnetic fields along with other well-defined physical parameters (Fuselier et al., 2011). In contrast, nightside reconnection is much less understood. Here, the solar wind-magnetosphere interaction stretches the dipole field lines in the antisunward direction forming the magnetotail while storing energy in the magnetic field. The release of this stored energy via reconnection is often unsteady and spontaneous. Observations of substorms (Russell & McPherron, 1973; Hones Jr., 1984; Baker et al., 1996; Angelopoulos et al., 2008, 2013) suggest that new X-lines form in the tail at distances of 10–30R_E and that this distance is controlled by the solar wind input (Nagai et al., 2005). However, despite decades of debate and being the target of dedicated satellite missions (Nagai et al., 2005; Angelopoulos et al., 2008; Burch et al., 2016), the factors that determine the emergence, location, size, and shape of nightside X-lines remain a major mystery in heliophysics.

The recent four-probe Magnetospheric MultiScale (MMS) mission (Burch et al., 2016) enabled microscopic analysis of magnetotail reconnection down to electron gyroradius scales (Torbert et al., 2018). During four years of MMS observations, 26 potential X-line encounters were found in the magnetotail (A. J. Rogers et al., 2019; A. Rogers et al., 2021), where explosive reconnection causes substorms (Angelopoulos et al., 2008; Angelopoulos et al., 2020; Sitnov et al., 2019). They were detected in the form of Ion Diffusion Regions (IDRs) characterized by reversals of the North-South component of the magnetic field, B_z, and of the Sun-Earth component of the proton bulk flow velocity, v_x, (Fig. 1 inset).

In this study, the global structure of magnetotail reconnection is derived from a large set of historic satellite magnetometer measurements using an advanced data mining approach. We show that our technique provides evidence justifying the global reconnection structure: the obtained contours delineating B_z reversals pass through most of the micro-scale IDRs discovered by MMS. We further discuss implications of the obtained magnetotail picture to the multiscale structure of its current sheet, and then describe its uncertainty and in-situ validation errors. Throughout this study, vector quantities are represented in the Geocentric Solar Magnetospheric System (GSM).

2 Data Mining Solution of the Data Paucity Problem

The key to solving the data paucity problem lies in the recurrent nature and repeatable pattern of storms and substorms. The storm recurrence time for medium intensity storms is approximately two weeks (Reyes et al., 2021), while it is 2–4 h for periodic substorm (Borovsky & Yakymenko, 2017). This repeatability allows the magnetic field to be reconstructed not only from observations at the moment of interest but also from records identified via mining the space magnetometer archive by searching for other times when the magnetosphere was in a similar global state. The magnetospheric state is characterized using geomagnetic indices (metrics of magnetic activity derived from networks of ground magnetometers) and solar wind conditions. Specifically, the magnetospheric state is defined using a 5-D state-space vector, $\mathbf{G}(t) = (G_1, ..., G_5)$, formed from the geomagnetic storm index (*SMRc*), substorm index (*SML*), their time derivatives, and the solar wind electric field parameter (vB_z^{IMF}; where v is the solar wind speed and B_z^{IMF} is the North-South component of the Interplanetary Magnetic Field, IMF). The *SMR* and *SML* (*SMRc* is a pressure-corrected *SMR* (Tsyganenko et al., 2021)) indices are provided by the SuperMag project (Gjerloev, 2012) and represent variations of the ground-based magnetometer records from low/mid- and high-latitude stations respectively analogous to the *Sym-H* and *AL* indices used before (Sitnov et al., 2008; G. K. Stephens et al., 2019). $G_{1-5}(t)$ are normalized by their standard deviations, smoothed over storm or substorm scales, and sampled at a 5-min cadence, as is detailed in (G. K. Stephens & Sitnov, 2021) and in the Supporting Information (SI). Including the time derivatives of these activity indices allows the data mining (DM) procedure to differentiate between storm and substorms phases as well as capturing memory effects of the magnetosphere as a dynamic system

(Sitnov et al., 2001). The space magnetometer archive contains data from 22 satellites (including the four MMS probes) spanning the years 1995–2020 resulting in 8,649,672 magnetic field measurements after being averaged over 5 and 15 min time windows as is further described in Figure S1 and Table S1 of the SI.

The DM algorithm employed is based on the k-nearest neighbor (kNN) classifier method (Wettschereck et al., 1997; Sitnov et al., 2008). To illustrate the algorithm, assume the magnetic field reconstruction, $\mathbf{B}(t)$, is sought for a query time $t = t^{(q)}$. This corresponds to a particular point in the 5-D state-space, $\mathbf{G}^{(q)} = \mathbf{G}(t^{(q)})$. Surrounding this point will be other points, $\mathbf{G}^{(i)}$, in close proximity to it; i.e., its nearest neighbors (NNs). Distances between points in state-space are computed using the Euclidean metric: $R_i = |\mathbf{G}^{(i)} - \mathbf{G}^{(q)}|$. Time-adjacent NNs form intervals in time that identify a subset of the magnetometer database used to fit the analytical formulation of the magnetic field, yielding $\mathbf{B}(t^{(q)})$. The specific choice of the number of NNs to use in the reconstruction, k_{NN}, is dictated by a balance between over- and under-fitting. G. K. Stephens and Sitnov (2021) found the optimal number to be $k_{NN} = 32,000$ for tail reconstructions of substorms, corresponding to $\sim 1\%$ of the total database. The resulting subset is composed of a very small number ($\sim$ 1–10) of real (from the event of interest) but many ($\sim 10^5$) virtual (from other events) satellites.

The large number of virtual points enables new magnetic field architectures (Tsyganenko & Sitnov, 2007; G. K. Stephens et al., 2019), which differ from classical empirical models with custom-tailored modules (e.g., Tsyganenko & Sitnov, 2005) by utilizing regular basis function expansions for the major magnetospheric current systems, to be used for the reconstructions. In particular, all near-equatorial currents are approximated by two expansions representing general current distributions of thick and thin current sheets with different thickness parameters D and D_{TCS}. The latter accounts for the formation of ion-scale thin current sheets (TCS) prior to substorm onset (V. Sergeev et al., 2011), as is further detailed below. The independence of the current sheet expansions is provided by the constraint $D_{TCS} < D$. To improve the reconstructions, while fitting the magnetic field model with the NN subset, the spacecraft data were additionally weighted: in the real space (to mitigate the inhomogeneity of their radial distribution (Tsyganenko & Sitnov, 2007)) and in the state-space (to reduce the uncertainty and bias toward weaker activity regions (G. K. Stephens & Sitnov, 2021)) as it is further detailed in the SI.

The resulting DM reconstruction of the magnetic field during the early expansion phase of the 5 August 2020 substorm (Figure 1) reveals the formation of an X-line at $r \approx 23R_E$ in the tail. This data-derived image of the X-line resembles sketches of solar flare arcades (e.g., Shiota et al., 2005) but with a fundamental advantage that it is backed by a quantitative description. The X-line appears on the dusk flank of the tail illustrated as the earthward part of the $B_z = 0$ isocontour in the equatorial plane (black line). It also corresponds to an earthward edge of a relatively long ($25R_E$) spiral structure, shown by the sample field lines that encircle the tailward part of the $B_z = 0$ isocontour and form a magnetic O-line. The large green sphere in Figure 1 indicates the location of the MMS satellites at this moment with the inset, which shows the observed B_z and v_x, demonstrating it was one of the fortuitous IDR encounters.

3 Ion Diffusion Regions

The main goal of the MMS mission (Burch et al., 2016) was the detection and investigation of reconnection regions in the magnetosphere and its boundary. That goal was relatively easy to achieve at the magnetopause because of its regular structure (Fuselier et al., 2011) and in the magnetosheath due to multiple reconnection sites in its turbulent plasma volume (Phan et al., 2018). By contrast, only a handful of fortunate X-line encounters were detected/investigated in the magnetotail (Torbert et al., 2018; Chen et al., 2019). In this regard, the proposed DM reconstructions offer an attractive opportunity to explore the dynamics of magnetotail topology on a global scale, and its fidelity can be demonstrated by comparing our results with MMS observations. Magnetic reconnection can be directly observed if and when a spacecraft fortuitously flies through an Ion Diffusion Region (IDR), as shown in Figure 1. A recent systematic survey of MMS plasma and

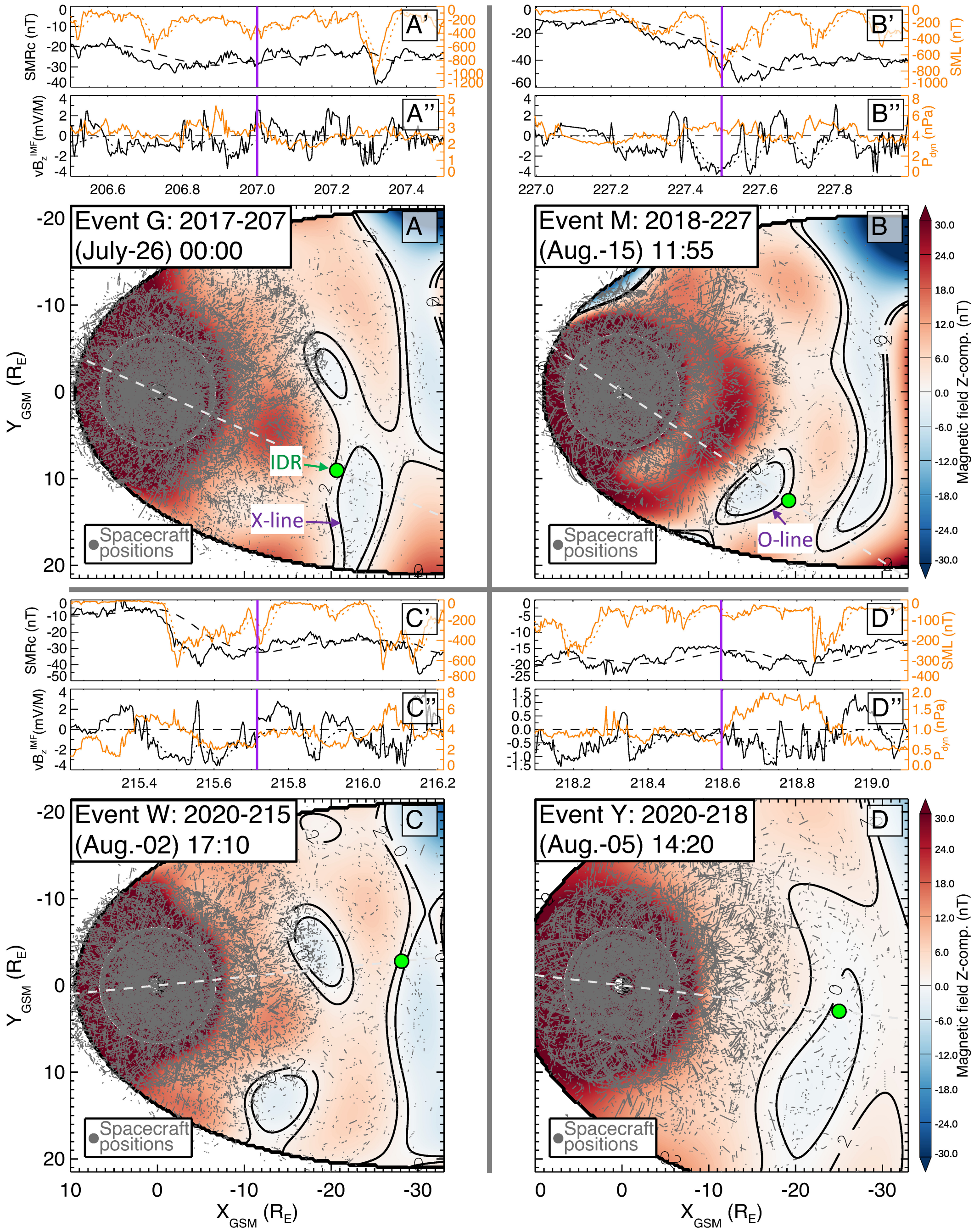

Figure 2. IDRs and the equatorial magnetic field landscape. (A–D) Color-coded distributions of the equatorial magnetic field, B_z, with $B_z = 0$ and 2 nT isocontours (black lines), big green dots pointing to the IDRs, and gray dots showing the spacecraft positions for the NN subsets used in the DM method for four IDR events, G, M, W and Y. Panels on top of each equatorial B_z distribution show the global context of the considered events in terms of (A'–D') the storm and substorm indices *SMRc* (black), *SML* (orange), and (A''–D'') the solar wind/IMF parameters vB_z^{IMF} (black) and P_{dyn} (orange) with the purple vertical line marking the event time.

field data in 2017 (A. J. Rogers et al., 2019) identified 12 such magnetotail IDRs, defined as correlated reversals of the proton bulk flow velocity, v_x, and the North-South magnetic field, B_z, as shown in the Figure 1 inset, along with additional Hall magnetic and electric field signatures. That analysis was later extended to 2018–2020 for a total of 26 IDR events (A. Rogers et al., 2021) labeled here A–Z, “IDR alphabet”, listed in Table S2 in the SI.

Figure 1 shows that the DM reconstruction correctly identifies one of the IDR regions, namely event Y (5 August 2020 14:20 UT), whose v_x and B_z reversals are shown in the inset. The projection of the magnetic field at the center of the tail current sheet into the equatorial plane is displayed in Figure 2D showing that the $B_z = 0$ contour passes within $\sim 1R_E$ of the IDR observed by MMS. This success is remarkable given that only $\sim 0.03\%$ of the measurements used to reconstruct the magnetic field were taken from this event, with the other 99.97% coming from other similar events identified using the above described DM approach. Below we show that similar $B_z = 0$ contours pass through most of the microscale IDRs discovered by MMS.

3.1 Reconstructed X- and O-lines in the Equatorial Plane

The reconstructions of 3 other events (G, M, W) presented in Figure 2 also show the $B_z = 0$ contours pass within $\sim 1R_E$ of the observed IDRs (the exact distances are provided in Table S2). Closer examination shows that only events G, W, and Y are X-lines, whereas event M corresponds to an O-line. Indeed, since the microscale formation of the MMS tetrahedron cannot determine X-line motions using timing analysis, (e.g., Eastwood et al., 2010), or by framing the X-lines by being tailward and earthward of them (Angelopoulos et al., 2008), it cannot distinguish whether they are X- or O-lines.

The equatorial X-line reconstructions for the remaining 22 IDR events are provided in Figs. S3–S8. They reveal that the DM approach hits 16 of the 26 IDRs (Figs. 2 and S3–S5), that is, the $B_z = 0$ contours pass within $\lesssim 2R_E$ of the IDRs, which includes 11 X-lines and 5 O-lines. Another 8 events are near hits, that is, the IDRs are located within $\lesssim 2R_E$ from $B_z = 2$ nT contours (Figs. S6 and S7). Only in 2 events (B, F) do the reconstructed $B_z = 0$ contours miss their IDR targets (Figure S8); however, both events have a plausible explanation. Event B occurs during weak magnetospheric activity ($SML \approx 0$) with effectively no solar wind/IMF input ($vB_z^{IMF} > 0$) while event F takes place during the middle of a several hours long gap in solar wind and IMF data (they are interpolated in the reconstruction).

3.2 Reconnection Features in the Meridional Planes

The corresponding meridional slices through the planes containing the IDRs of the Figure 2 events (G, M, W, Y) are shown in Figure 3, illustrating the magnetic topology and distributions of electric currents, while the remainder of the IDR alphabet (Figures S3–S8) is shown in Figures S9–S14. The figures clarify that the observed $B_z = 0$ contours indeed represent X- and O-lines similar to the 3D magnetotail field geometry shown in Figure 1. They also confirm the quasi-2-D nature of reconnection apparently imposed by the North-South symmetry of the magnetotail (e.g., Tsyganenko & Fairfield, 2004) which is drastically different from the inherently 3-D reconnection processes in the solar corona (Liu et al., 2016) and rapidly rotating planets (Griton et al., 2018).

These meridional distributions resemble empirical visualizations of reconnection in laboratory plasmas, which became possible due to their large number of real probes (up to 200) and additional symmetry constraints, such as the cylindrical symmetry imposed by the toroidal-shaped flux cores in the PPPL Magnetic Reconnection Experiment (MRX) (Ji et al., 2022). Still, in contrast to MRX, magnetotail reconnection is only quasi 2-D due to the finite length of the X-line forming a closed loop with the O-line, as well as the explicit 3-D effects, such as null-points (e.g., Greene, 1988; Ji et al., 2022). Null-points in the tail were indeed inferred from the four-probe Cluster observations (Xiao et al., 2006). An example of the null-point pair seen in our DM reconstruction of event Y is presented in Figure S15. Additional deviations from the simple 2-D

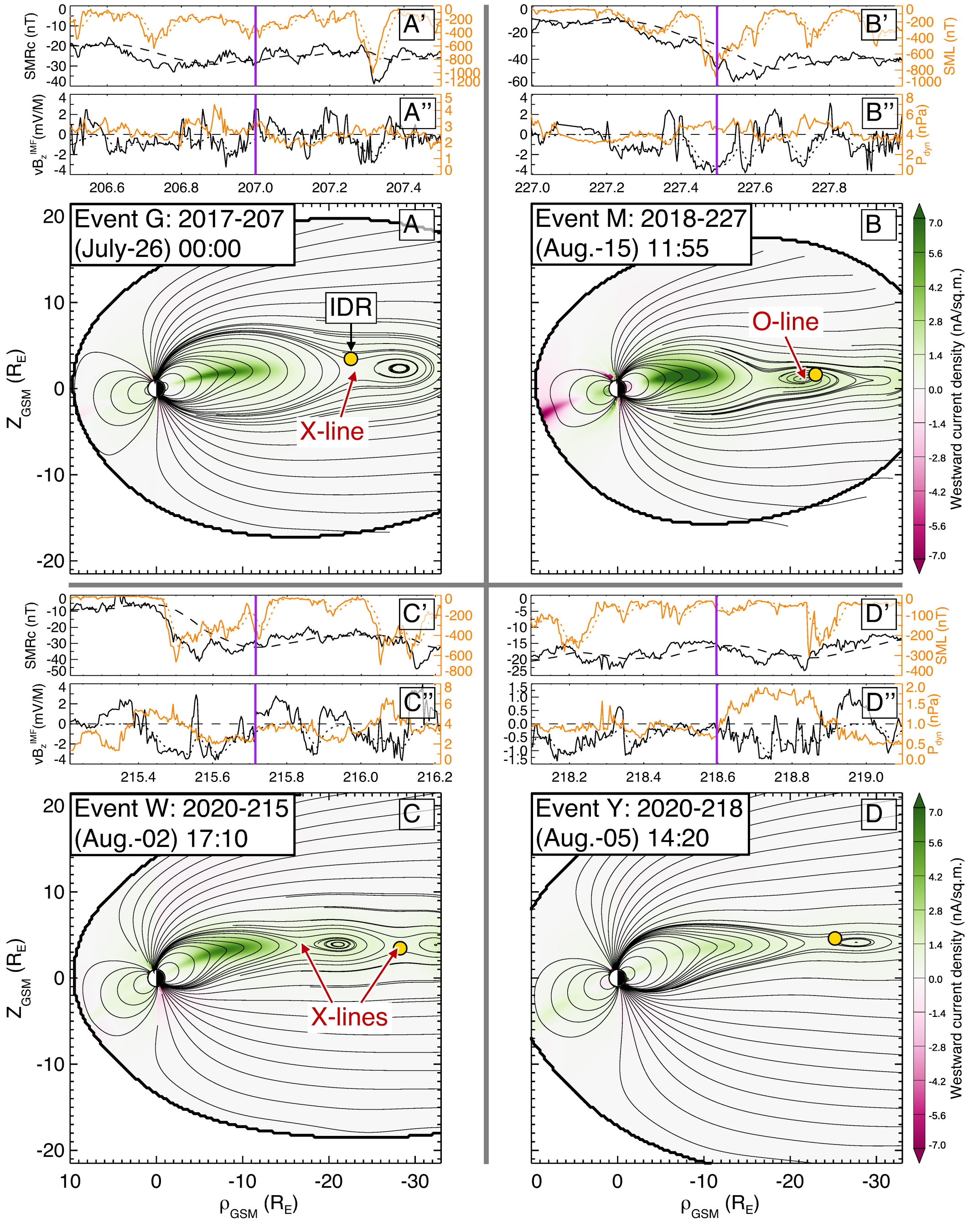

Figure 3. IDRs against the meridional current and magnetic field distributions. (A–D) Color-coded distribution of the electric current perpendicular (westward positive) to the meridional plane, which contains the corresponding IDR (white dashed lines in Figure 2), for four events shown in Figure 2 with the similar format for global parameters (A'–D') and (A"–D") on top of each distribution. The IDRs are shown here by big orange dots. Thin and thick lines show the magnetic field lines and the magnetospheric boundary (magnetopause).

picture could be due to a strong IMF B_y (e.g., Cowley, 1981) or North-South oscillations of the tail current sheet that resemble a flapping flag (e.g., V. A. Sergeev et al., 2006; Sitnov et al., 2019).

Note that in the present reconstructions the original multiscale tail model (G. K. Stephens et al., 2019) with the embedded TCS structure has been further generalized to verify the possible physical mechanisms of the TCS formation. It can be explained, (e.g., Sitnov et al., 2006), by figure-eight like Speiser (1965) proton orbits. If this is the case, the parameter D_{TCS} of the magnetic field model should depend on the distance ρ from the Earth because the Speiser orbit size, ρ_{Si}, is inversely proportional to the magnetic field outside the sheet, B_L, which itself depends on ρ (Wang et al., 2004). To take this effect into account the magnetic field architecture was further generalized using the approximation $D_{TCS}(\rho) = [D_*^{-1} + \alpha \exp(-\beta\rho)]^{-1}$ with free parameters α, β and D_* to be inferred from data. The fitting details provided in Figure S2 suggest that the scaling $D_{TCS} \propto B_L^{-1} \propto \rho_{Si}$ does indeed take place, which supports the theoretical mechanism of the TCS formation related to the Speiser orbits.

4 Validation and Uncertainty Quantification

An example of in-situ validation of this global reconstruction, rarely possible because of the data paucity, is shown in Figs. 4A–4D for the MMS magnetic field observations of the tail during event Y. It reveals relatively large deviations in the magnetic field components $B_{x,y}$ parallel to the current plane (Figs. 4A, 4B). They are likely caused by the flapping North-South motions of the current sheet as a whole (V. A. Sergeev et al., 2006) that were found in MMS observations as well (Farrugia et al., 2021). These motions are spontaneous and may appear in different phases of activity, so it is not surprising that they are not captured by the DM reconstructions. At the same time, the B_z magnetic field is reproduced even better than it appears in observations after 5-min averages (compare the black line in Figure 4C with the inset in Figure 1). Thus, hitting 24 out of 26 IDRs, achieved in this study, shows (i) how to overcome the curse of data paucity for in-situ data and (ii) presents solid evidence that not only validates our DM reconstructions, but also helps understand the reconnection mechanisms and its consequences.

The fidelity of the present reconstructions can also be seen from the uncertainty analysis presented in Figs. 4E–I. It compares 5 original binning parameters of the magnetosphere with their means and standard deviations over the NN bins. The closeness of means to the original parameters G_{1-5} and small relative values of deviations suggest that the selected NNs closely follow the magnetospheric dynamics, especially on substorm scales (Figs. 4G–4H).

5 Conclusions

This picture of the 2017–2020 MMS IDR alphabet suggests that, in spite of the extreme paucity of in-situ observations, DM successfully reconstructs the overall structure of magnetotail X- and O-lines because they are strongly self-organized on the global scale. The X-lines vary in length from 5 to $40R_E$, with the shorter ones forming inside of $\sim 20R_E$ while the longer ones, $\sim 40R_E$, appear beyond $25R_E$. The concurrent appearance of such near-Earth and midtail X-lines is consistent with the original conjectures regarding new X-line formation during substorms (Hones Jr., 1984). It also explains the detection of X-lines as discrete points in radial distance in remote sensing (Angelopoulos et al., 2013, Fig. 3C) as well as the stepwise retreat of magnetic reconnection regions suggested by their auroral manifestations and confirmed by in-situ observations (Ieda et al., 2016). The persistent formation of X-lines near $30R_E$ has also been confirmed by the statistical analysis of the travelling compression regions (Imber et al., 2011). The success of our X-line reconstruction indicates that year after year, the spatial/temporal patterns of storms and substorms in the Earth's magnetotail are highly recurrent and hence reproducible with historic data, while magnetic reconnection controls the global state of the magnetosphere reflected in its activity indices, their trends, and the solar wind energy input.

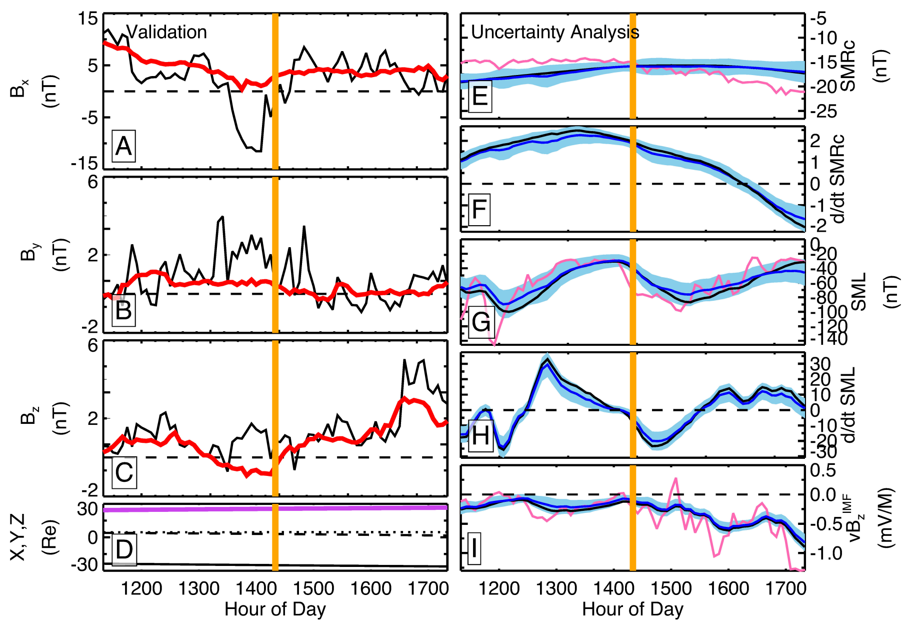

Figure 4. Validation and uncertainty analysis for event Y. (A)–(C) The 5-min averaged GSM magnetic field components (black lines) and their DM reconstructions (red lines). (D) MMS ephemeris (in GSM) X (solid line), Y (dashed line), Z (dash-dotted line) and the radial distance (pink line). (E)–(I) The storm/substorm state binning parameters $\langle SMRc|$, $D\langle SMRc|/Dt$, $\langle SML|$, $D\langle SML|/Dt$, and $\langle vB_s^{IMF}|$ as described in the SI, shown by black lines as compared to their means over the NNs (blue lines). The light blue shading shows the standard deviations $\pm 1\sigma$ of the NNs. Pink lines in Figs. 4E, 4G, and 4I show the original 5-min OMNI data for the parameters *SMRc* (pressure-corrected *SMR* (Tsyganenko et al., 2021)), *SML*, and vB_z^{IMF}. Yellow bars show the moment of the spatial reconstruction 5 August 2020, 14:20 UT shown in Figs. 1, 2D and 3D.

6 Open Research

The data used in the paper are archived on Zenodo (G. Stephens et al., 2022). For each of the 26 IDR events, files are included that detail: time intervals identified using the nearest-neighbor search and the resulting subset of magnetometer data and their associated weights, files containing the fit set of coefficients and parameters for the model, and the digital model output data that were used in constructing the figures. The compiled magnetometer database used in this study is available on the SPDF website (Korth et al., 2018). This study extended this database with the addition of MMS magnetometer data which has also been included in the Zenodo archive. The SMR and SML indices obtained from the SuperMAG web page are also included in the Zenodo archive. The data describing the solar wind conditions were taken from the 5-min OMNI data (Papitashvili & King, 2020).

Acknowledgments

The authors acknowledge useful discussions with G. Clark, R. Nakamura, S. Sharma, H. Spence, V. Titov, J. Vandegriff, D. Vassiliadis, and J. Zhang. They thank the SuperMag team and their collaborators, which provided the global indices of the storm and substorm activity. They also thank the teams who created and provided Geotail, Polar, IMP 8, Cluster, THEMIS, Van Allen Probes, MMS and GOES data obtained via NSSDC CDAWeb online facility, as well as Wind and ACE solar wind/IMF data that went into the production of the OMNI data obtained via NASA/GSFC's Space Physics Data Facility's OMNIWeb service. This work was funded by NASA grants 80NSSC19K0074, 80NSSC20K1271, 80NSSC20K1787, as well as NSF grants AGS-1702147 and AGS-1744269. N. A. Tsyganenko acknowledges support of the RFBR grant 20-05-00218.

References

Angelopoulos, V., Artemyev, A., Phan, T. D., & Miyashita, Y. (2020, January). Near-Earth magnetotail reconnection powers space storms. *Nature Physics*, *16*(3), 317-321. doi: 10.1038/s41567-019-0749-4

Angelopoulos, V., McFadden, J. P., Larson, D., Carlson, C. W., Mende, S. B., Frey, H., ... Kepko, L. (2008). Tail reconnection triggering substorm onset. *Science*, *321*(5891), 931–935. Retrieved from `https://science.sciencemag.org/content/321/5891/931` doi: 10.1126/science.1160495

Angelopoulos, V., Runov, A., Zhou, X.-Z., Turner, D. L., Kiehas, S. A., Li, S.-S., & Shinohara, I. (2013). Electromagnetic energy conversion at reconnection fronts. *Science*, *341*(6153), 1478–1482. Retrieved from `https://science.sciencemag.org/content/341/6153/1478` doi: 10.1126/science.1236992

Baker, D. N., Pulkkinen, T. I., Angelopoulos, V., Baumjohann, W., & McPherron, R. L. (1996). Neutral line model of substorms: Past results and present view. *Journal of Geophysical Research: Space Physics*, *101*(A6), 12975-13010. doi: 10.1029/95JA03753

Birn, J., Hesse, M., & Schindler, K. (1996). Mhd simulations of magnetotail dynamics. *Journal of Geophysical Research: Space Physics*, *101*(A6), 12939-12954. doi: https://doi.org/10.1029/96JA00611

Borovsky, J. E., & Yakymenko, K. (2017). Substorm occurrence rates, substorm recurrence times, and solar wind structure. *Journal of Geophysical Research: Space Physics*, *122*(3), 2973-2998. doi: https://doi.org/10.1002/2016JA023625

Burch, J. L., Moore, T. E., Torbert, R. B., & Giles, B. L. (2016, March). Magnetospheric Multiscale Overview and Science Objectives. *Space Science Reviews*, *199*(1-4), 5-21. doi: 10.1007/s11214-015-0164-9

Burch, J. L., Torbert, R. B., Phan, T. D., Chen, L.-J., Moore, T. E., Ergun, R. E., ... Chandler, M. (2016). Electron-scale measurements of magnetic reconnection in space. *Science*, *352*(6290), 10.1126/science.aaf2939. Retrieved from `https://science.sciencemag.org/content/352/6290/aaf2939` doi: 10.1126/science.aaf2939

Camporeale, E. (2019). The challenge of machine learning in space weather: Nowcasting and forecasting. *Space Weather*, *17*(8), 1166-1207. doi: https://doi.org/10.1029/2018SW002061

Chen, L.-J., Wang, S., Hesse, M., Ergun, R. E., Moore, T., Giles, B., … Lindqvist, P.-A. (2019). Electron diffusion regions in magnetotail reconnection under varying guide fields. *Geophysical Research Letters*, *46*(12), 6230-6238. doi: https://doi.org/10.1029/2019GL082393

Childs, H., Brugger, E., Whitlock, B., Meredith, J., Ahern, S., Pugmire, D., … Navrátil, P. (2012, October). Visit: An end-user tool for visualizing and analyzing very large data. In *High performance visualization–enabling extreme-scale scientific insight* (p. 357-372). doi: 10.1201/b12985

Cowley, S. (1981). Magnetospheric asymmetries associated with the y-component of the IMF. *Planetary and Space Science*, *29*(1), 79-96. Retrieved from `https://www.sciencedirect.com/science/article/pii/0032063381901410` doi: https://doi.org/10.1016/0032-0633(81)90141-0

Dungey, J. W. (1961). Interplanetary magnetic field and the auroral zones. *Phys. Rev. Lett.*, *6*, 47–48. Retrieved from `https://link.aps.org/doi/10.1103/PhysRevLett.6.47` doi: 10.1103/PhysRevLett.6.47

Eastwood, J. P., Phan, T. D., Øieroset, M., & Shay, M. A. (2010). Average properties of the magnetic reconnection ion diffusion region in the earth's magnetotail: The 2001-2005 Cluster observations and comparison with simulations. *Journal of Geophysical Research: Space Physics*, *115*(A8), https://doi.org/10.1029/2009JA014962. doi: https://doi.org/10.1029/2009JA014962

Farrugia, C. J., Rogers, A. J., Torbert, R. B., Genestreti, K. J., Nakamura, T. K. M., Lavraud, B., … Dors, I. (2021). An encounter with the ion and electron diffusion regions at a flapping and twisted tail current sheet. *Journal of Geophysical Research: Space Physics*, *126*(3), e2020JA028903. doi: https://doi.org/10.1029/2020JA028903

Fuselier, S. A., Trattner, K. J., & Petrinec, S. M. (2011). Antiparallel and component reconnection at the dayside magnetopause. *Journal of Geophysical Research: Space Physics*, *116*(A10), https://doi.org/10.1029/2011JA016888. Retrieved from `https://agupubs.onlinelibrary.wiley.com/doi/abs/10.1029/2011JA016888` doi: https://doi.org/10.1029/2011JA016888

Gjerloev, J. W. (2012). The supermag data processing technique. *Journal of Geophysical Research: Space Physics*, *117*(A9), https://doi.org/10.1029/2012JA017683. doi: https://doi.org/10.1029/2012JA017683

Greene, J. M. (1988). Geometrical properties of three-dimensional reconnecting magnetic fields with nulls. *Journal of Geophysical Research: Space Physics*, *93*(A8), 8583-8590. doi: https://doi.org/10.1029/JA093iA08p08583

Griton, L., Pantellini, F., & Meliani, Z. (2018). Three-dimensional magnetohydrodynamic simulations of the solar wind interaction with a hyperfast-rotating uranus. *Journal of Geophysical Research: Space Physics*, *123*(7), 5394-5406. doi: https://doi.org/10.1029/2018JA025331

Hones Jr., E. W. (1984). Magnetic reconnection in space and laboratory plasmas. In (p. 178-184). American Geophysical Union. doi: https://doi.org/10.1029/GM030p0178

Ieda, A., Nishimura, Y., Miyashita, Y., Angelopoulos, V., Runov, A., Nagai, T., … Machida, S. (2016). Stepwise tailward retreat of magnetic reconnection: Themis observations of an auroral substorm. *Journal of Geophysical Research: Space Physics*, *121*(5), 4548-4568. doi: https://doi.org/10.1002/2015JA022244

Imber, S. M., Slavin, J. A., Auster, H. U., & Angelopoulos, V. (2011). A themis survey of flux ropes and traveling compression regions: Location of the near-earth reconnection site during solar minimum. *Journal of Geophysical Research: Space Physics*, *116*(A2), https://doi.org/10.1029/2010JA016026. doi: https://doi.org/10.1029/2010JA016026

Ji, H., Daughton, W., Jara-Almonte, J., Le, A., Stanier, A., & Yoo, J. (2022). Magnetic reconnection in the era of exascale computing and multiscale experiments. *Nature Re-*

views Physics, *4*, 263–282. doi: 10.1038/s42254-021-00419-x

Korth, H., Sitnov, M., & Stephens, G. (2018). *Magnetic field modeling database description final* [dataset]. NASA Space Physics Data Facility. Retrieved from `https://spdf.gsfc.nasa.gov/pub/data/aaa_special-purpose-datasets/empirical-magnetic-field-modeling-database-with-TS07D-coefficients/`

Liu, R., Kliem, B., Titov, V. S., Chen, J., Wang, Y., Wang, H., ... Wiegelmann, T. (2016, feb). STRUCTURE, STABILITY, AND EVOLUTION OF MAGNETIC FLUX ROPES FROM THE PERSPECTIVE OF MAGNETIC TWIST. *The Astrophysical Journal*, *818*(2), 148. Retrieved from `https://doi.org/10.3847/0004-637x/818/2/148` doi: 10.3847/0004-637x/818/2/148

Nagai, T., Fujimoto, M., Nakamura, R., Baumjohann, W., Ieda, A., Shinohara, I., ... Mukai, T. (2005). Solar wind control of the radial distance of the magnetic reconnection site in the magnetotail. *Journal of Geophysical Research: Space Physics*, *110*(A9), https://doi.org/10.1029/2005JA011207. Retrieved from `https://agupubs.onlinelibrary.wiley.com/doi/abs/10.1029/2005JA011207` doi: https://doi.org/10.1029/2005JA011207

Papitashvili, N. E., & King, J. H. (2020). *Omni 5-min data* [dataset]. NASA Space Physics Data Facility. Retrieved from `https://www.unavco.org/data/doi/10.7283/633E-1497` doi: 10.48322/gbpg-5r77

Phan, T. D., Eastwood, J. P., Shay, M. A., Drake, J. F., Sonnerup, B. U. Ö., Fujimoto, M., ... Magnes, W. (2018, May 01). Electron magnetic reconnection without ion coupling in Earth's turbulent magnetosheath. *Nature*, *557*(7704), 202-206. Retrieved from `https://doi.org/10.1038/s41586-018-0091-5` doi: 10.1038/s41586-018-0091-5

Reyes, P. I., Pinto, V. A., & Moya, P. S. (2021). Geomagnetic storm occurrence and their relation with solar cycle phases. *Space Weather*, *19*(9), e2021SW002766. doi: https://doi.org/10.1029/2021SW002766

Rogers, A., Farrugia, C. J., Torbert, R. B., & Rogers, T. J. (2021). Applying magnetic curvature to to MMS data to identify thin current sheets relative to tail reconnection. *Earth and Space Science Open Archive*, 12. doi: 10.1002/essoar.10509282.1

Rogers, A. J., Farrugia, C. J., & Torbert, R. B. (2019). Numerical algorithm for detecting ion diffusion regions in the geomagnetic tail with applications to mms tail season 1 may to 30 september 2017. *Journal of Geophysical Research: Space Physics*, *124*(8), 6487-6503. Retrieved from `https://agupubs.onlinelibrary.wiley.com/doi/abs/10.1029/2018JA026429` doi: https://doi.org/10.1029/2018JA026429

Russell, C. T., & McPherron, R. L. (1973, Nov 01). The magnetotail and substorms. *Space Science Reviews*, *15*(2), 205-266. Retrieved from `https://doi.org/10.1007/BF00169321` doi: 10.1007/BF00169321

Sergeev, V., Angelopoulos, V., Kubyshkina, M., Donovan, E., Zhou, X.-Z., Runov, A., ... Nakamura, R. (2011). Substorm growth and expansion onset as observed with ideal ground-spacecraft themis coverage. *Journal of Geophysical Research: Space Physics*, *116*(A5), https://doi.org/10.1029/2010JA015689. doi: https://doi.org/10.1029/2010JA015689

Sergeev, V. A., Sormakov, D. A., Apatenkov, S. V., Baumjohann, W., Nakamura, R., Runov, A. V., ... Nagai, T. (2006). Survey of large-amplitude flapping motions in the midtail current sheet. *Annales Geophysicae*, *24*(7), 2015–2024. Retrieved from `https://angeo.copernicus.org/articles/24/2015/2006/` doi: 10.5194/angeo-24-2015-2006

Shiota, D., Isobe, H., Chen, P. F., Yamamoto, T. T., Sakajiri, T., & Shibata, K. (2005, nov). Self-consistent magnetohydrodynamic modeling of a coronal mass ejection, coronal dimming, and a giant cusp-shaped arcade formation. *The Astrophysical Journal*, *634*(1), 663–678. Retrieved from `https://doi.org/10.1086/496943` doi: 10.1086/496943

Sitnov, M., Birn, J., Ferdousi, B., Gordeev, E., Khotyaintsev, Y., Merkin, V., ... Zhou, X. (2019, June). Explosive Magnetotail Activity. *Space Science Reviews*, *215*(4), 31. doi:

10.1007/s11214-019-0599-5

Sitnov, M. I., Sharma, A. S., Papadopoulos, K., & Vassiliadis, D. (2001, Dec). Modeling substorm dynamics of the magnetosphere: From self-organization and self-organized criticality to nonequilibrium phase transitions. *Phys. Rev. E*, *65*, 016116. Retrieved from `https://link.aps.org/doi/10.1103/PhysRevE.65.016116` doi: 10.1103/PhysRevE.65.016116

Sitnov, M. I., Stephens, G. K., Tsyganenko, N. A., Miyashita, Y., Merkin, V. G., Motoba, T., … Genestreti, K. J. (2019). Signatures of nonideal plasma evolution during substorms obtained by mining multimission magnetometer data. *Journal of Geophysical Research: Space Physics*, *124*(11), 8427-8456. doi: 10.1029/2019JA027037

Sitnov, M. I., Swisdak, M., Guzdar, P. N., & Runov, A. (2006). Structure and dynamics of a new class of thin current sheets. *Journal of Geophysical Research: Space Physics*, *111*(A8), https://doi.org/10.1029/2005JA011517. doi: https://doi.org/10.1029/2005JA011517

Sitnov, M. I., Tsyganenko, N. A., Ukhorskiy, A. Y., & Brandt, P. C. (2008). Dynamical data-based modeling of the storm-time geomagnetic field with enhanced spatial resolution. *Journal of Geophysical Research: Space Physics*, *113*(A7), 10.1029/2007JA013003. doi: 10.1029/2007JA013003

Speiser, T. W. (1965). Particle trajectories in model current sheets: 1. analytical solutions. *Journal of Geophysical Research (1896-1977)*, *70*(17), 4219-4226. doi: https://doi.org/10.1029/JZ070i017p04219

Stephens, G., Sitnov, M., Weigel, R., Turner, D., Tsyganenko, N., Rogers, A., … Slavin, J. (2022). *Global structure of magnetotail reconnection revealed by mining space magnetometer data* [dataset]. Zenodo. Retrieved from `https://doi.org/10.5281/zenodo.6862829` doi: 10.5281/zenodo.6862829

Stephens, G. K., & Sitnov, M. I. (2021). Concurrent empirical magnetic reconstruction of storm and substorm spatial scales using data mining and virtual spacecraft. *Frontiers in Physics*, *9*, 210. Retrieved from `https://www.frontiersin.org/article/10.3389/fphy.2021.653111` doi: 10.3389/fphy.2021.653111

Stephens, G. K., Sitnov, M. I., Korth, H., Tsyganenko, N. A., Ohtani, S., Gkioulidou, M., & Ukhorskiy, A. Y. (2019). Global empirical picture of magnetospheric substorms inferred from multimission magnetometer data. *Journal of Geophysical Research: Space Physics*, *124*(2), 1085-1110. Retrieved from `https://agupubs.onlinelibrary.wiley.com/doi/abs/10.1029/2018JA025843` doi: 10.1029/2018JA025843

Torbert, R. B., Burch, J. L., Phan, T. D., Hesse, M., Argall, M. R., Shuster, J., … Saito, Y. (2018). Electron-scale dynamics of the diffusion region during symmetric magnetic reconnection in space. *Science*, *362*(6421), 1391–1395. Retrieved from `https://science.sciencemag.org/content/362/6421/1391` doi: 10.1126/science.aat2998

Tsyganenko, N. A., Andreeva, V. A., Sitnov, M. I., Stephens, G. K., Gjerloev, J. W., Chu, X., & Troshichev, O. A. (2021). Reconstructing substorms via historical data mining: Is it really feasible? *Journal of Geophysical Research: Space Physics*, *126*(10), e2021JA029604. doi: https://doi.org/10.1029/2021JA029604

Tsyganenko, N. A., & Fairfield, D. H. (2004). Global shape of the magnetotail current sheet as derived from geotail and polar data. *Journal of Geophysical Research: Space Physics*, *109*(A3), https://doi.org/10.1029/2003JA010062. doi: https://doi.org/10.1029/2003JA010062

Tsyganenko, N. A., & Sitnov, M. I. (2005). Modeling the dynamics of the inner magnetosphere during strong geomagnetic storms. *Journal of Geophysical Research: Space Physics*, *110*(A3). doi: 10.1029/2004JA010798

Tsyganenko, N. A., & Sitnov, M. I. (2007). Magnetospheric configurations from a high-resolution data-based magnetic field model. *Journal of Geophysical Research: Space Physics*, *112*(A6), 10.1029/2007JA012260. doi: 10.1029/2007JA012260

Wang, C.-P., Lyons, L. R., Nagai, T., & Samson, J. C. (2004). Midnight radial profiles of the quiet and growth-phase plasma sheet: The geotail observations. *Journal of Geophysical Research: Space Physics*, *109*(A12), https://doi.org/10.1029/2004JA010590. doi: https://doi.org/10.1029/2004JA010590

Wettschereck, D., Aha, D. W., & Mohri, T. (1997, Feb 01). A review and empirical evaluation of feature weighting methods for a class of lazy learning algorithms. *Artificial Intelligence Review*, *11*(1), 273-314. Retrieved from `https://doi.org/10.1023/A:1006593614256` doi: 10.1023/A:1006593614256

Xiao, C. J., Wang, X. G., Pu, Z. Y., Zhao, H., Wang, J. X., Ma, Z. W., … Escoubet, C. P. (2006, Jul 01). In situ evidence for the structure of the magnetic null in a 3d reconnection event in the earth's magnetotail. *Nature Physics*, *2*(7), 478-483. Retrieved from `https://doi.org/10.1038/nphys342` doi: 10.1038/nphys342